J. Fluid Mech. (1993), *vol.* 257, *pp.* 339–357

Time-dependent thermocapillary convection in a rectangular cavity: numerical results for a moderate Prandtl number fluid

By L. J. PELTIER† AND S. BIRINGEN
Department of Aerospace Engineering Sciences, University of Colorado, Boulder, CO, USA

(Received 13 July 1992 and in revised form 24 May 1993)

The present numerical simulation explores a thermal–convective mechanism for oscillatory thermocapillary convection in a shallow rectangular cavity for a Prandtl number 6.78 fluid. The computer program developed for this simulation integrates the two-dimensional, time-dependent Navier–Stokes equations and the energy equation by a time-accurate method on a stretched, staggered mesh. Flat free surfaces are assumed. The instability is shown to depend upon temporal coupling between large-scale thermal structures within the flow field and the temperature sensitive free surface. A primary result of this study is the development of a stability diagram presenting the critical Marangoni number separating the steady from the time-dependent flow states as a function of aspect ratio for the range of values between 2.3 and 3.8. Within this range, a minimum critical aspect ratio near 2.3 and a minimum critical Marangoni number near 20000 are predicted, below which steady convection is found.

1. Introduction

Thermocapillary convection is fluid motion driven by surface tension differences resulting from thermal gradients along a fluid's free surface. For many fluids, surface tension is a decreasing function of temperature, hence, warm regions of fluid yield to cooler regions to generate a surface flow. Although, previous experimental and theoretical studies have shown the existence of steady and time-dependent convection states, the present study is the first to obtain solutions for unsteady surface tension driven flow (using the flat free surface) producing estimates for the critical Marangoni number, Ma_c, as a function of aspect ratio, Ar. In the present paper, Ma_c refers to the Marangoni number for the onset of oscillatory motion.

Recent attention to the thermocapillary problem has been spawned by the prospect of containerless materials processing in the low-gravity environment. Specifically, containerless growth of semiconductor crystals in space has been considered as a way to reduce convection in crystal melts and to avoid contamination from crucible walls. As buoyant forces are reduced, however, thermocapillary forces remain as the dominant mechanism to drive fluid motion. It is, therefore desirable to understand parameter ranges within which different thermocapillary flow states will exist in order to improve control of the fluid environment surrounding a growing crystal. Specifically, it is important to understand under which conditions a thermocapillary flow will exhibit time-dependent behaviour.

A rich body of experimental data describing the nature of time-dependent

† Present address: Department of Meteorology, Pennsylvania State University, State College, Pennsylvania, PA 16802, USA.

thermocapillary convection are available for the cylindrical floating half zones confirming the existence of the oscillatory time-dependent state and showing that the mechanism for oscillation is independent of buoyancy. Using fluids with Prandtl numbers Pr, of order 10, Velten, Schwabe & Scharmann (1991) have experimentally estimated Ma_c to be of order 10^4 and have demonstrated a dependence of Ma_c on Ar. Experimental studies have also indicated a strong Pr dependence of the oscillatory state. For silicon oils with $100 < Pr < 400$, Chun (1980) found that the onset of oscillatory convection could be related to the development of an S-shaped temperature profile along the thermocapillary surface. As a precursor to oscillation, however, this profile was not observed experimentally by Jurisch (1990) in liquid metals having $Pr = 0.025$. Additional distinctions between oscillatory thermocapillary flows at large and small Pr were demonstrated by Velten *et al.* (1991). Their work showed that two distinct modes of instability may be observed depending upon the Pr of the test fluid. In a cylindrical floating half zone, the preferred mode of oscillation for materials with $Pr < 50$ is an azimuthally travelling disturbance, whereas, the preferred mode of oscillation for materials with $Pr > 50$ is an axially travelling disturbance. Kamotani, Ostrach & Vargas (1984), however, have demonstrated that azimuthal periodicity is not a mechanistic requirement for oscillations in fluids of $Pr < 50$. After bisecting a cylindrical floating half zone of hexadecane ($Pr = 42$) with a thin plastic plate thereby removing azimuthal periodicity, oscillatory flow was observed in each of the resulting semi-circular columns.

Among the theoretical investigations of the oscillatory thermocapillary phenomena, Smith & Davis (1983) used the analytic profile for steady, parallel, thermocapillary flow in a long, thin, rectangular cavity developed in the asymptotic analysis by Sen & Davis (1982) as a basic state for their linear perturbation analysis. Arguing that a thermal–convective mechanism for the oscillatory instability will be insensitive to surface deformation, Smith & Davis (1983) retain the flat free-surface assumption. An infinite Ar is also assumed. Their results qualitatively reproduced the seemingly disparate characteristics of oscillatory thermocapillary convection observed in experiments. The linear study by Smith & Davis (1983) together with the weakly nonlinear analysis by Smith (1988) discloses that the thermocapillary system is most susceptible to an oblique unsteady hydrothermal wave whose angle of propagation relative to the basic state was a function of Pr. The angle of propagation of this oblique hydrothermal wave is nearly perpendicular to the basic state for low Pr materials and is nearly parallel to the basic state for high Pr materials. Thus the azimuthal dependence of low Pr fluids and the axial dependence for high Pr fluid of the thermocapillary oscillations is predicted in accordance with experimental findings (Velten *et al.* 1991). The study of Smith & Davis (1983) using the thermal–convective, rectangular cavity model indicates that the relevant physics can be captured by the flat free-surface assumption. Their parallel flow and infinite Ar assumptions, however, do not apply to finite cavities.

The energy stability analysis by Shen *et al.* (1990) underscores the need to account for endwall effects. They consider an axisymmetric half-zone of finite length using the flat free-surface assumption. They compare their predictions of Ma_c for a $Pr = 1$ fluid against the experimental results of Preisser, Schwabe & Scharmann (1983) for a $Pr = 7$ fluid and show good agreement. In contrast, Xu & Davis (1984) present perturbation analysis results for a similar system of infinite Ar which differ from experiment by nearly two orders of magnitude.

Although the energy analysis and linear perturbation techniques may capture Ma_c, they cannot show the thermal–convective origin of the surface perturbation instigating

the oscillatory response nor the supercritical evolution of the instability. These can be addressed by full numerical simulation to give a complete description of the oscillatory thermocapillary response.

Full numerical simulations of thermocapillary convection in a square cavity have been provided by Zebib, Homsy & Meiburg (1985) and Carpenter & Homsy (1990). These studies have confirmed the boundary-layer structure of thermocapillary flows inferred from asymptotic studies, however, no link to time-dependent thermocapillary convection states could be found. Carpenter & Homsy (1990) considered the linear stability of their numerical solutions over a broad range of Pr at Ma well beyond the critical 20000 to 30000 estimated by the experiments of Preisser *et al.* (1983) and Kamotani *et al.* (1984) and found no unstable modes; however, they did not consider the effects of cavity aspect ratio. Ben Hadid & Roux (1990) also sought time-dependence in a layer of a $Pr = 0.015$ fluid over a range of Ar and found no evidence of oscillatory behaviour. Their low-Prandtl-number fluid, however, is expected to behave differently to the $Pr = 6.78$ material used in the present study.

Other studies in the literature address time-dependence in the context of buoyant/thermocapillary convection. Among these Ben Hadid & Roux (1992) consider a $Pr = 0.015$ fluid, and Villers & Platten (1992) consider time-dependence in acetone both experimentally ($Pr = 4.24$) and numerically ($Pr = 4.0$). This interaction between buoyant and thermocapillary forces is not the primary focus of this work.

The present work provides a fully nonlinear direct numerical simulation of oscillatory thermocapillary convection for a Prandtl number 6.78 fluid focusing on the thermal–convective mechanism considered by Smith & Davis (1983). Oscillatory convection is found in this fluid layer using the flat free-surface assumption. Through our simulations, the transition between stationary and oscillatory convection is extensively investigated; a stability diagram is developed presenting the critical (Ar, Ma) combinations separating time-dependent from steady thermocapillary flows. In addition, a physical description of the thermocapillary oscillation is provided relating the temporal interaction between large-scale thermal structures and the temperature-sensitive free surface.

2. Mathematical formulation

We consider an incompressible fluid with a flat free surface filling an open, two-dimensional rectangular cavity under zero-gravity conditions. A schematic of this model is presented in figure 1. Although some deformation of the fluid free-surface is anticipated under these conditions, both Smith & Davis (1983) and Shen *et al.* (1990) have shown that the flat free-surface assumption captures the relevant physics. Also, Smith & Davis (1983) have shown that the anticipated mode of instability for our $Pr = 6.78$ fluid is a travelling oblique roll with primarily transverse character which can be captured by the two-dimensional model. We further assume that the bounding cross-flow walls are far from the location of the chosen cross-section so that three-dimensionality from viscous interactions with these walls will be weak.

The left and right walls of the cavity are heated and cooled, respectively, while the bottom of the cavity and the free surface are insulated. The aspect ratio of the cavity, Ar, is defined as the ratio of the length of the cavity, L_x, to the depth of the fluid layer, L_y, and is written $Ar = L_x/L_y$.

The mathematical equations governing this system are the incompressible Navier–Stokes equations together with the thermal energy equation. In non-dimensional form, these are written

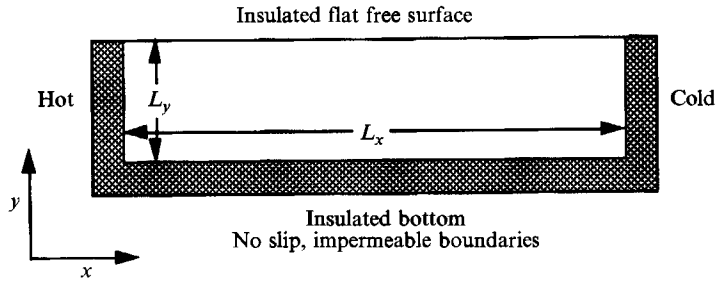

FIGURE 1. Model schematic of the thermocapillary Cartesian cavity with aspect ratio, Ar. The left-hand and right-hand sidewalls are heated and cooled, respectively, while the bottom and free surface are insulated. A flat free surface is enforced.

Continuity

$$\nabla \cdot \boldsymbol{u} = 0, \tag{1}$$

Momentum

$$\frac{\mathrm{D}\boldsymbol{u}}{\mathrm{D}t} = -\nabla p + \frac{Pr}{Ma}\nabla^2 \boldsymbol{u}, \tag{2}$$

Energy

$$\frac{\mathrm{D}\theta}{\mathrm{D}t} = \frac{1}{Ma}\nabla^2 \theta, \tag{3}$$

where the non-dimensional variables $\boldsymbol{u}$, θ, and p, represent the velocity vector, temperature, and pressure, respectively. The characteristic quantities selected for the non-dimensionalization are the horizontal lengthscale, L_x, the sidewall temperature difference, $\Delta T = T_{hot} - T_{cold}$, and the thermocapillary velocity, $V_r = \sigma_T \Delta T/\mu$. From these, the characteristic timescale is defined as L_x/V_r, and the non-dimensional temperature is defined as $\theta = (T - T_{avg})/\Delta T$, where $T_{avg} = \frac{1}{2}(T_{hot} + T_{cold})$. The thermophysical properties appearing in the formulation of the present problem are the dynamic viscosity, μ, the kinematic viscosity, ν, the thermal diffusivity, κ, and the thermal coefficient of surface tension, σ_T.

At each solid wall of the cavity, no-slip and impermeability conditions are enforced on the tangential and normal velocity components. These are written

$$\boldsymbol{u} = 0. \tag{4}$$

At the upper free surface, $y = Ar^{-1}$, the kinematic constraint,

$$v = 0, \tag{5}$$

is imposed on the vertical velocity, and the shear stress balance is satisfied by the horizontal velocity, u. This tangential stress balance is written

$$\frac{\partial u}{\partial y} = -\frac{\partial \theta}{\partial x} \tag{6}$$

and may be interpreted as a balance between shear stresses at the free surface and thermocapillary stresses along the surface. Shear contributions from the passive gas bounding the fluid system have been neglected.

The isothermal sidewall conditions representing a hot left wall and a cold right wall are written

$$\theta = [1/2, 1/2] \quad \text{at } x = [0, 1], \tag{7}$$

	Shear driven cavity (mesh resolution) $\lvert\psi_c\rvert$					
Re_s	Peltier & Biringen		Biringen & Danabasoglu		*Kim & Moin (1985) **Ghia *et al.* (1982)	
1	0.0992	(33 × 33)	0.0992	(33 × 33)	0.099*	(65 × 65)
400	0.111	(33 × 33)	0.107	(33 × 33)	0.114**	(257 × 257)
	Thermally driven cavity (mesh resolution) $\lvert\psi_{max}\rvert$					
R_a	Peltier & Biringen		Biringen & Danabasoglu		de Vahl Davis (1983)	
10^5	9.58	(33 × 33)	9.78	(33 × 33)	9.612	(benchmark)

TABLE 1. Comparison of shear driven cavity and thermally driven cavity calculations. The streamfunction at the core of the primary vortex, $|\psi_c|$, and the maximum streamfunction, $|\psi_{max}|$, are compared.

while the insulating conditions at the top and bottom of the cavity are

$$\frac{\partial\theta}{\partial y} = 0 \quad \text{at} \quad y = [0, Ar^{-1}]. \tag{8}$$

The general, flat free-surface, thermocapillary problem is completely described by the Marangoni, Ma, and Prandtl, Pr, numbers which reflect the contributions of thermocapillarity and viscous to thermal diffusion. Their definitions are

$$Ma = \frac{\sigma_T \Delta T L_x}{\mu\kappa}, \quad Pr = \frac{\nu}{\kappa}. \tag{9}$$

The thermocapillary Reynolds number, Re, is sometimes used instead of the Marangoni number to parameterize thermocapillary results. This parameter is defined as $Re = Ma/Pr$. For data presentation, the streamfunction, ψ, integrated Nusselt number, Nu, and surface Reynolds number, Re_s, information are extracted from the calculated velocity and temperature fields. The definitions for these quantities are

$$\frac{\partial\psi}{\partial x} = -v, \tag{10}$$

$$Nu(x) = \int_0^{Ar^{-1}} \left[u\theta - \frac{1}{Ma}\frac{\partial\theta}{\partial x}\right] dy, \tag{11}$$

and

$$Re_s = \frac{u_s L_x}{\nu}, \tag{12}$$

where u_s is a surface velocity. With insulating conditions at the top and bottom, the integrated Nusselt number across the cavity must be constant for time-independent solutions. For these cases, the measure of convergence that we have considered is the root-mean-square value of the difference between two successive (in time) values of the horizontal velocity; convergence is assumed when this quantity becomes less than 10^{-7}. For simulations resulting in oscillatory responses, convergence is determined by the approach to a statistically steady state. A measure of this condition is the amplitude

differences of a field variable over each period of oscillation scaled by its average magnitude also over the period of oscillation. Statistical convergence is assumed when this value becomes less than 10^{-7}.

3. Solution procedure and code validation

The governing equations are solved on a stretched, staggered mesh using second-order finite differences and time-splitting. Detailed descriptions of the time-splitting scheme and of the spatial descretization of the nonlinear convective terms are given by Biringen & Danabasoglu (1989), Kim & Moin (1985), and Le & Moin (1991).

The implicit Crank–Nicolson method is used to temporally discretize the linear diffusive terms, and the explicit, three-step, third-order Runge–Kutta time advancement (Le & Moin 1991) is implemented for the nonlinear convective terms. All the spatial derivatives are approximated by second-order central finite differences. Previous numerical simulations of cavity flows (Kim & Moin 1985; Biringen & Danabasoglu 1989; Huser & Biringen 1992) have conclusively demonstrated that for the time-stepping procedure employed in the present work, central differences used on the convective terms do not cause any numerical oscillations even at high Reynolds and Rayleigh numbers.

Use of the Runge–Kutta advancement relaxes the convective stability constraint allowing stable computations at larger Courant numbers (thereby larger timestep increments) than methods like Adams–Bashforth extrapolation. Each time advancement, however, requires the integrating of the governing equations three times, thereby tripling the *CPU* expense of the scheme. Experience with the Runge–Kutta method has shown that a ten-fold increase in the timestep over that dictated by explicit stability considerations may be realized without degrading the accuracy of the numerical solutions, therefore, the overall increase in *CPU* efficiency for the Runge–Kutta method is approximately a factor of three.

The Helmholtz equations and the pressure Poisson equation resulting from the above discretization are solved using the tensor product (eigenvalue decomposition) technique. Complete details of this solution procedure are found in Peltier, Biringen & Chati (1990) and Huser & Biringen (1992).

Each calculation is started using the results of a previously converged solution of a nearby parameter set as an initial guess accelerating convergence to the new statistically steady state. Sensitivity of the final solution to the initial conditions is checked by also converging some solutions from a quiescent velocity profile and a conductive thermal profile. Identical solutions were found.

Timestep increment independence is assured by decreasing the timestep size between solutions until the maximum absolute value of the streamfunction stabilized to 6 digits. In addition, grid resolution independence is checked by comparing solutions on a coarse grid with solutions on a finer grid. Within this work, coarse grid resolution refers to a 45×45 mesh with a cosine stretching in each direction, and high-grid resolution refers to a 63×63 mesh also with a cosine stretching in each direction. For example, a highly resolved layer would have a 63×63 mesh resolution with a minimum Δx of 6.4×10^{-4} and a minimum Δy of $\Delta x Ar^{-1}$.

The accuracy of the numerical code is established by comparing driven cavity solutions with previously published results. Table 1 compares results for shear driven cavity and thermally driven cavity calculations against results presented by Biringen & Danabasoglu (1989) including the results of Kim & Moin (1985) and the benchmark calculations of Ghia, Ghia & Shin (1982) and de Vahl Davis (1983). Very good

	Thermocapillary driven cavity (mesh resolution)					
	$Pr = 1$, $Re = 10000$		$Pr = 30$, $Re = 2000$		$Pr = 50$, $Re = 1000$	
	C&H (1990) (74 × 74)	P&B (31 × 31)	C&H (1990) (74 × 74)	P&B (74 × 74)	C&H (1990) (64 × 64)	P&B (74 × 74)
ψ_{min}	3.23×10^{-3}	3.24×10^{-3}	2.24×10^{-3}	1.82×10^{-3}	1.77×10^{-3}	1.44×10^{-3}
ω_{core}	6.97×10^{-2}	7.29×10^{-2}	7.71×10^{-2}	6.53×10^{-2}	7.57×10^{-2}	6.01×10^{-2}
u_{mid}	2.96×10^{-2}	3.06×10^{-2}	2.00×10^{-2}	1.61×10^{-2}	1.43×10^{-2}	1.16×10^{-2}
0.0	4.36	4.30	6.53	7.14	5.77	6.09
Nu 0.5	4.33	4.36	6.40	6.71	5.79	5.84
1.0	4.40	4.44	6.84	6.69	5.82	5.76

TABLE 2. Comparison of thermocapillary driven cavity calculations with the results of Carpenter & Homsy (1990).

agreement is found in both cases verifying the accuracy of the solution procedure. The thermocapillary driven cavity is considered in table 2, and the results are compared to calculations by Carpenter & Homsy (1990) for Prandtl numbers 1, 30 and 50 providing very good agreement. For all the computations reported in this paper, the solution procedure satisfies divergence-free velocity field to machine accuracy.

4. Results and discussion

The present parametric results are organized into four sections. The first section presents a stability diagram for pure thermocapillary convection as a function of Marangoni number, *Ma*, and aspect ratio, *Ar*, which separates a regime of oscillatory thermocapillary response from steady thermocapillary flows. Special interest is focused on a range of parameters arising in this diagram that have double valued stability limits. The second section offers a description of the physical process sustaining time-dependent thermocapillary convection and the third section offers a quantitative summary of the related surface effects. The final section considers physical interpretation of the stability diagram for example fluids.

We reduce the parameter space spanned by this study to a subset of (Ar, Ma) by restricting ourselves to a fluid with $Pr = 6.78$ which is representative of a large number of materials used in experiments. For example Velten *et al.* (1990) have often used sodium nitrate $NaNO_3$, with a *Pr* of 8.86 and Villers & Platten (1992) have used acetone with a *Pr* between 3.73 and 4.25. It should be noted that the same unsteady mechanism was revealed for a $Pr = 23.0$ fluid which is discussed by Peltier & Biringen (1992). Consequently, we can assert that these mechanisms can generalize to a range of *Pr*.

For the following discussion, a cavity of fixed length is assumed, hence, *Ar* reflects the depth of the fluid layer. Since the independent control parameter in *Ma* is the product $\Delta T L_x$, changes in *Ma* reflect corresponding changes in ΔT which drives the thermocapillary flow.

4.1. *The stability diagram*

To construct the stability diagram, critical (Ar, Ma) combinations separating steady from time-dependent thermocapillary response regimes are found using the stream-function, ψ, data from super-critical simulations. In the oscillatory regime, time-dependent thermocapillary flow is characterized by a primary convection cell throughout the oscillation cycle. Using ψ_{min} and ψ_{max} to denote the minimum and

maximum values of ψ at the core of this cell over the oscillation cycle, the fluctuation amplitude, $\Delta\psi$, is defined as $(\psi_{max}-\psi_{min})$, and the average strength, ψ_{AVG}, is defined as $\frac{1}{2}(\psi_{max}+\psi_{min})$. As the critical value of either Ar or Ma is approached from within the unsteady regime, $\Delta\psi$ decreases, becomes zero at the critical curve. This approach is valid when the bifurcation is supercritical, which is the case in the present work. Thus a scheme to predict the critical value of Ma, Ma_c is constructed by quadratic extrapolation of $(Ma, \Delta\psi)$ data to $\Delta\psi = 0$ for a fixed Ar. Similarly, for a fixed Ma, the critical Ar is found by extrapolation. We base this scheme on the parameter $\Delta\psi$ since we can calculate this value with a high degree of certainty and since it provides a measure of the strength of the oscillation. This procedure is similar to the scheme used by Pulicani, del Arco & Peyret (1990) to predict the critical Grashof number for the onset of oscillatory buoyant convection in liquid metals. The accuracy of the predicted critical parameters is validated by spot-checking (Ar, Ma) combinations near the estimated critical value.

The ψ data from a large number of time-dependent simulations were collected and a representative subset is presented in table 3. Since the characteristic velocity scales and timescales are functions of Ma, here, and in the rest of this work, ψ data and the period of oscillation, Π, have been scaled by Ma and Ma^{-1}, respectively, to remove the Ma dependence. The ψ data presented are derived from time histories over an oscillation cycle. An example is offered in figure 2 which presents the ninth and tenth periods of oscillation for the simulation corresponding to the (Ar, Ma) parameter combination (2.6, 50000). Dotted lines are used to bound ψ_{max} and ψ_{min} which are incident with the maxima and minima in both periods showing that the flow field has reached a statistically steady state. Since the cell has a negative sense of rotation, ψ_{min} denotes the instant of greatest strength, and ψ_{max} denotes the instant of least strength. The time difference between successive maxima in the ψ time history defines Π.

Successive maxima in the ψ history are also used to define a coordinate system for temporal data. The instants 0 and 2π are defined to correspond to the maxima in the oscillation cycle, and π is equally spaced in time from these instants. Since temporal asymmetry exists in the evolution of the primary convection cell, π does not correspond to the position of maximum strength. The asymmetry, however, is weak, and instant π is rarely far from the position of maximum strength. In table 3, values of the maximum and midpoint surface Reynolds number on the fluid free surface at instant π in the oscillation cycle are also presented. One other quantity, x_θ, is tabulated which is defined later in this discussion.

Typically, the evolution to a statistically steady solution, figure 2, is characterized by long transients. Experience has shown that to converge a flow field using the results from a nearby supercritical parameter set as initial conditions, approximately nine periods of oscillation are required before a true statistically steady state is reached. The minimum number of cycles necessary to converge a flow field increases with increasing Ma. The uniqueness of the solutions was verified by converging the extreme thermocapillary case, (3.8, 135200), from both the results of a nearby parameter set and from a conductive thermal profile and a quiescent velocity field. Identical solutions were obtained. The possibility of hysteresis with respect to time-dependence was also explored by simulating the near critical parameter set $(Ar, Ma) = (3.4, 40000)$ using both oscillatory and steady initial conditions. Again, identical solutions were found; thus, to within the resolution of this numerical approach, hysteresis is not predicted.

When possible we chose to use previous unsteady solutions as initial conditions for new runs, since the integration time required to reach either statistical or absolute convergence of the new solution was significantly shorter than if we had used the

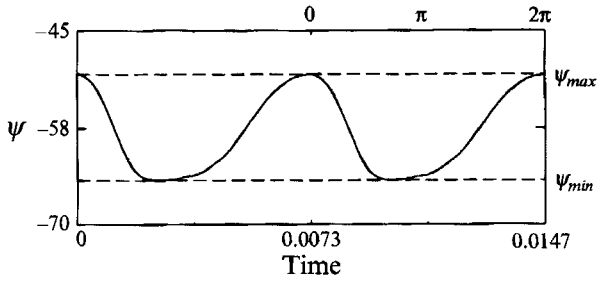

FIGURE 2. Time history of the core strength of the primary convection cell over approximately two periods of oscillation for the oscillatory (*Ar*, *Ma*) parameter combination (2.6, 50000).

Ar	*Ma* ($\times 10^{-3}$)	*Ma* ψ_{AVG}	*Ma* $\Delta\psi$	Π/Ma ($\times 10^{3}$)	x_θ	*Ma Re*$_s$ (*Max*)	*Ma Re*$_s$ (*Mid*)	Δt	Grid
2.6	30	37.17	6.486	9.310	0.578	493.4	18.11	0.049	45 × 45
	40	48.16	10.90	8.234	0.603	645.4	34.95	0.051	45 × 45
	50	57.53	13.48	7.344	0.652	774.4	87.35	0.051	45 × 45
	60	64.69	12.21	6.588	0.711	895.7	124.4	0.051	45 × 45
	65	67.98	11.60	6.262	0.735	957.6	137.3	0.055	45 × 45
	70*	69.80	4.953	5.736	0.770	1028.0	139.4	0.055	45 × 45
	75*	73.13	1.871	5.339	—	—	—	0.056	45 × 45
	100*	90.88	0.03660	4.225	—	—	—	0.065	45 × 45
3.8	50	41.09	4.204	3.798	0.397	726.3	19.82	0.020	63 × 63
	60	47.84	7.536	3.583	0.471	848.1	33.03	0.050	45 × 45
	75	58.18	12.49	3.417	0.475	976.5	0.4800	0.050	45 × 45
	135.2	93.71	34.49	3.370	0.500†	1935.0	83.48	0.025	63 × 63

* This simulation represents a decaying solution which was not converged to statistically steady state. Values for ψ_{AVG} and $\Delta\psi$, therefore, are lower and upper bounds, respectively.

† Approximate value.

A complete table for other *Ar* is available from the authors.

TABLE 3. Tabulated data for unsteady simulations of a *Pr* 6.78 fluid; the ψ_{AVG} is the average core strength of the primary convection, $\Delta\psi$, is the fluctuation amplitude, Π is the period of oscillation, Re_s is the surface Reynolds number (based on either the maximum surface velocity, u_{max}, or the mid-point surface velocity, u_{mid}, at instant π) and Δt is the computational timestep. Streamfunction data have been scaled by *Ma* and Π has been scaled by Ma^{-1}.

results of a steady calculation as initial conditions. This behaviour arises from a very long integration time between the onset of the oscillatory disturbance and its reaching appreciable amplitude.

The approximate stability diagram separating regions of time-dependent thermocapillary response from steady thermocapillary flows constructed from the results of fully nonlinear numerical simulations is presented in figure 3. Here, the contours represent constant $\Delta\psi$ at contour intervals of 5.0 as functions of *Ar* and *Ma* for *Ar* up to 3.8. The critical curve corresponds to the zero contour. In figure 3, simulated parameter combinations are shown as open and filled circles where open circles denote steady solutions and filled circles denote time-dependent solutions.

Surprisingly good agreement is found between values of Ma_c along the lower branch of the stability curve (20000 to 40000) and the experimental results of Preisser *et al.* (1983) and Kamotani *et al.* (1984) which estimate Ma_c to lie between 20000 and 30000. Their data represent predictions for a floating half-zone where the effects of gravity

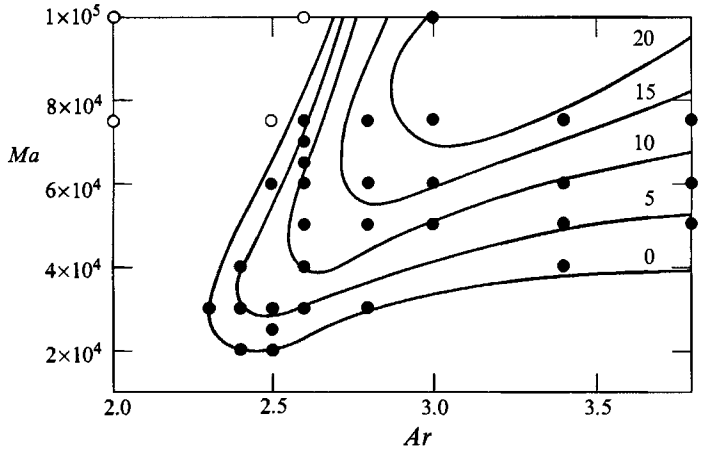

FIGURE 3. Stability diagram contouring the fluctuation amplitude of oscillation as a function of the combination (*Ar*, *Ma*). The zero contour represents the critical curve, and the contour interval is 5.0.

were minimized both by the small scales of the experiments and by the imposition of a stabilizing temperature gradient. This agreement suggests that the mechanism for instability is similar for the two geometries. The stability diagram also predicts that square cavities ($Ar = 1.0$) will not be susceptible to oscillatory behaviour which rationalizes the inability of Carpenter & Homsy (1990) to find oscillatory responses for square cavity simulations at comparable *Pr*.

The most interesting characteristic of the stability curve is that, over a range of parameters, it is double valued (i.e. it has both a lower and an upper branch). Within this range, a transition between steady and time-dependent thermocapillary flow will be experienced for both low and high values of the control parameter. Also within the parameter ranges investigated, time-dependence is not found below a critical *Ar* near 2.3 nor below an Ma_c near 20000. The upper branch of the stability diagram rises steeply with increasing *Ar* and may not exist above a second critical *Ar* near 3. The upper arm of the stability diagram will be discussed later in the text.

Susceptibility of a fluid system to time-dependence can be read from the stability diagram. For example, in an $Ar = 2.6$ cavity having sidewalls with equal temperatures, a quiescent state is expected. Increases in ΔT will drive steady thermocapillary flows, $\Delta\psi = 0$, until a transition to time dependence, $\Delta\psi > 0$, is experienced near $Ma =$ 23000. Above this Ma_c, the flow becomes oscillatory. Further increasing *Ma*, $\Delta\psi$ reaches a maximum near $Ma = 50000$. Above this value, increases in *Ma* lead to decreases in $\Delta\psi$ until near $Ma = 80000$, $\Delta\psi = 0$, and steady thermocapillary convection returns.

Evolution of ψ_{AVG}, $\Delta\psi$, and Π for this series is presented in figure 4. A near linear dependence between ψ_{AVG} and *Ma* is demonstrated in figure 4(*a*). This trend is consistent both in the time-dependent and steady regimes and is a direct consequence of the thermocapillary forcing, equation (7), on the temperature gradient at the free surface. Since larger values of *Ma* reflect larger ΔT and greater thermocapillary forces, increases in the convection strength are expected. Values of $\Delta\psi$ over the range of *Ma* are shown in figure 4(*b*). Extrapolations of the lower and upper values of Ma_c from these data points yield estimates 24000 and 77000, respectively. Finally, in figure 4(*c*), Π is shown to decrease as ΔT is raised. This behaviour of Π is indirect support that the thermal perturbation responsible for the oscillatory thermocapillary response is

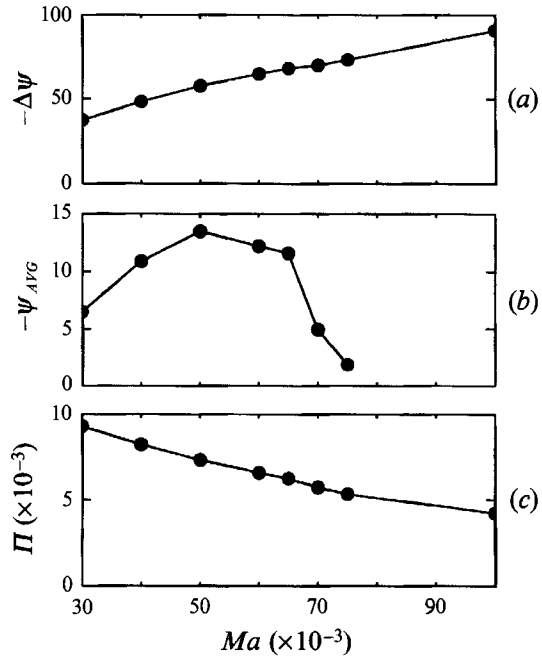

FIGURE 4. Simulation data as a function of the Marangoni number for aspect ratio 2.6: (*a*) average core cell strength, ψ_{AVG}, (*b*) fluctuation amplitude, $\Delta\psi$, and (*c*) period of oscillation, Π. ●, measured data points. In this figure, ψ_{AVG}, $\Delta\psi$ and Π are scaled by Ma as in table 3.

convective in nature. For a constant Ar cavity, the size of the primary convection cell is fixed, and increased strength of convection leads to decreased cell turnover time. Thus, the frequency of a convective perturbation is expected to increase in agreement with the shortened Π observed.

A very similar behaviour is found for the time-dependent response of a fluid system at constant ΔT and decreasing Ar. Variable Ar can be achieved in an open cavity by addition of fluid to the fluid layer. According to the stability diagram, figure 3, steady thermocapillary convection is expected for a thermocapillary layer of $Ar = 3$. Decreasing Ar by addition of fluid results in steady flow until a transition to time-dependence is experienced near $Ar = 2.8$. Below this critical Ar, $\Delta\psi$ grows in amplitude until a maximum is reached near $Ar = 2.5$. Further decreases in Ar lead to decreases in $\Delta\psi$ until near $Ar = 2.3$, $\Delta\psi = 0$, and steady thermocapillary convection returns. The ψ data for a representative parametric study of Ar with $Ma = 30000$ is presented in figure 5. As before, ψ_{AVG}, $\Delta\psi$, and Π are plotted in figures 5(*a*)–5(*c*), respectively.

The magnitude of ψ_{AVG} increases with decreasing Ar. Since the ΔT driving the flow is constant, the increase in convection is probably due to lessened viscous effects from the bounding walls in deeper cavities. The response of $\Delta\psi$ to the acceleration is similar, and the lower and upper critical values for Ar predicted from this curve are 2.8 and 2.3, respectively. An opposite response in Π is observed. With increase ψ_{AVG}, Π increases. This response also can be explained by a convective temperature perturbation. As Ar is decreased, the cell turnover distance also increases; if the corresponding acceleration of the flow is too weak, a decrease in the frequency of perturbation is anticipated leading to an increase in Π.

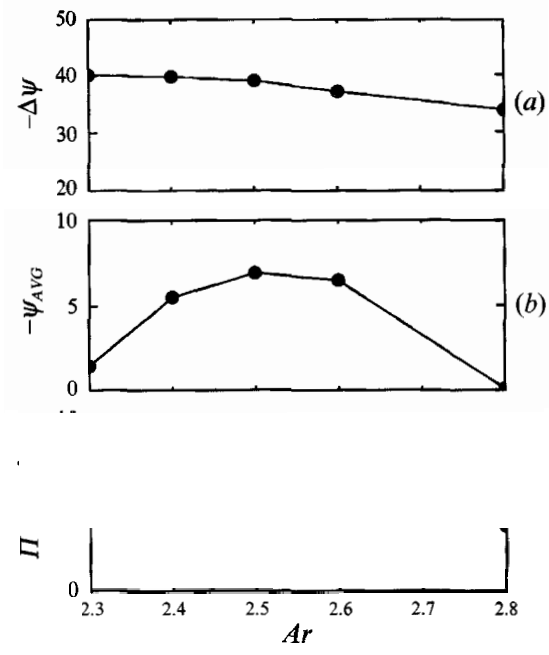

FIGURE 5. Simulation data as a function of the aspect ratio for Marangoni number, 30000: (*a*) average core cell strength, ψ_{AVG}, (*b*) fluctuation amplitude, $\Delta\psi$, and (*c*) period of oscillation, Π. ●, measured data points.

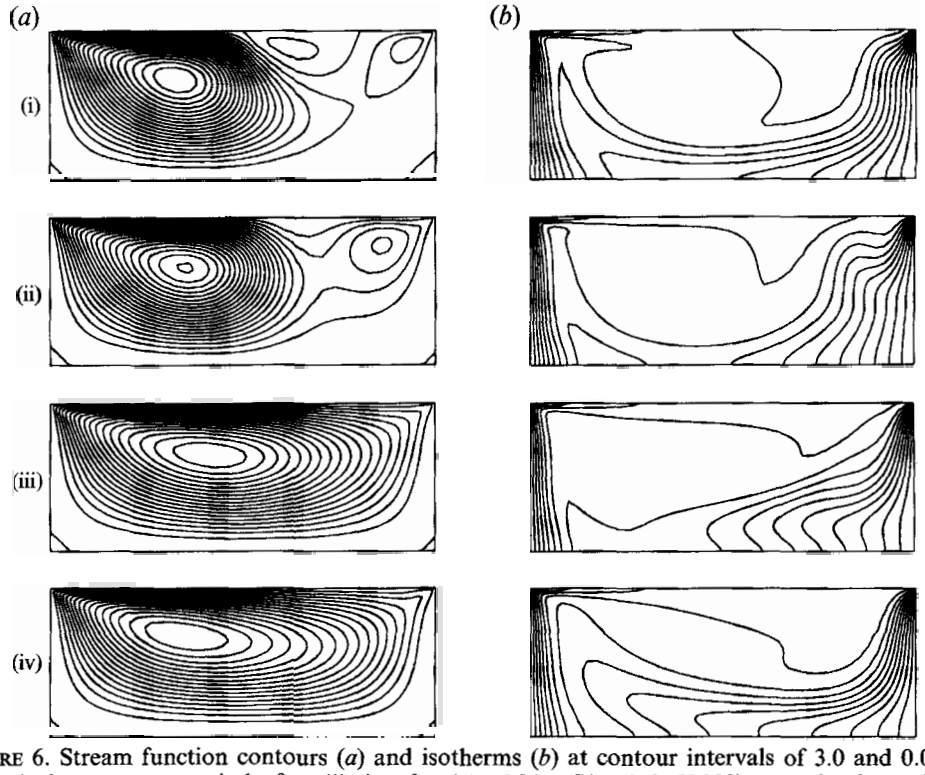

FIGURE 6. Stream function contours (*a*) and isotherms (*b*) at contour intervals of 3.0 and 0.0625, respectively, over one period of oscillation for (*Ar*, *Ma*) =S15 (2.6, 50000): samples from (i) $\frac{1}{2}\pi$, (ii) π, (iii) $\frac{3}{2}\pi$, and (iv) 2π.

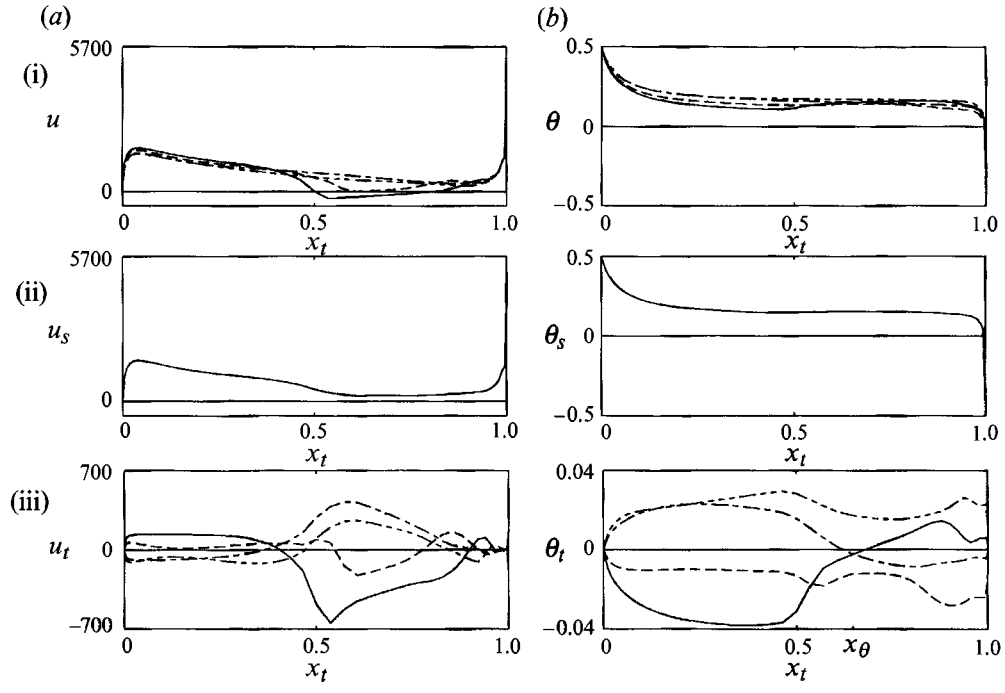

FIGURE 7. Surface profiles of horizontal velocity (*a*) and temperature (*b*) for (*Ar*, *Ma*) = (2.6, 50000) sampled at instants ——, $\frac{1}{2}\pi$, – – –, π, —·—, $\frac{3}{2}\pi$ and –··–, 2π, in the oscillation period: (i) total quantity, (ii) average, and (iii) fluctuation from average.

4.2. *Physical description of the oscillation*

Comparisons of the streamfunction contours and isotherms at the parameter combinations representing the maximum $\Delta\psi$, lower critical, and upper critical simulations demonstrate that a complete structural analogy exists in the evolution of flow with increasing *Ma* and with decreasing *Ar*. Thus the response of the thermocapillary system is concluded to be a function of the flow strength which is a function of *Ar* and *Ma*.

Streamfunction contours and isotherms are presented in figure 6 for $Ma = 50000$ leading to the maximum $\Delta\psi$ at $Ar = 2.6$. The instants $\frac{1}{2}\pi$, π, $\frac{3}{2}\pi$, and 2π are presented in figures 6(i)–6(iv), respectively. Views of the flow structure at zero and 2π are presented in figure 6(iv). This instant corresponds to the time of least strength in the cycle of the primary convection cell which has expanded to occupy the entire cavity. Its core is biased toward the hot wall in agreement with Carpenter & Homsy (1990) for steady thermocapillary flows in moderate Prandtl number fluids. At this instant, a monotonic temperature gradient exists along the free surface, figure 7(*b*) (i), indicating that the thermocapillary surface forces are directed toward the cold wall. Thermal boundary layers are observed near both sidewalls with the extreme isotherm compaction observed at the junction between the free surface and the cold wall. The weaker thermal boundary layer near the junction between the free surface and the hot wall sustains a large convection cell. Near the cold wall, a local acceleration is driven by an extreme isotherm compaction.

The clockwise sense of rotation of the primary cell allows cool fluid to be siphoned away from the cold wall along the bottom of the cavity. Near the hot wall, this cool stream is deflected upward satisfying continuity and creating a cool finger which

interacts with the thermocapillary surface from below. This cool finger maintains the thermal gradient near the hot wall.

For this parameter combination, the cool finger is sufficient to generate a thermal perturbation (local cooling) on the surface which instigates the oscillation. In response to the strengthened temperature gradient, the primary convection cell retracts toward the hot wall and strengthens, figure 6(i). As shear forces from the primary cell weaken near the cold wall, a secondary convection cell with the same sense of rotation appears accelerated by thermocapillary responses to the isotherm compaction. An additional, tertiary convection cell with a counterclockwise sense of rotation appears, sustained by shear forces from the primary and secondary convection cells and a weak adverse temperature gradient. It will be shown, however, that neither the secondary nor the tertiary cells are mechanistic requirements for the oscillation.

The primary and secondary convection cells strengthen until a maximum strength is reached (figure 6(ii)). In this flow field, two actions tend to re-establish the single-cell state. First, without being replenished by new fluid siphoned from the cold wall, the cool finger warms, and its influence on the surface is diminished. For this high-amplitude oscillation, a retraction of the cool finger is observed. Secondly, the increased strength of the primary cell pulls warm fluid from the hot wall extending the influence of thermocapillary forces closer toward the cold wall and allowing its expansion in this direction.

The secondary convection cell pulls cool fluid from the cold wall and ejects this fluid upward toward the thermocapillary surface. The surface is cooled, and the driving force for the secondary cell is diminished. Through this action, the secondary cell helps to extinguish itself, and the expansion of the primary convection cell is augmented. By instant $\frac{3}{2}\pi$ presented in figure 6(iii), the single cell state has been firmly reestablished, and the formation of a new cool finger begins.

4.3. *Quantitative description of surface effects*

Surface profiles for the non-dimensional horizontal velocity, u, and temperature, θ, sampled at instants $\frac{1}{2}\pi$, π, $\frac{3}{2}\pi$, and 2π are presented in figure 7. A profile of the total quantity is presented in figure 7(i) whereas the average profile, subscript s, and deviations from the average, subscript t, are presented in figures 7(ii) and 7(iii). Since this flow is thermocapillary driven, responses in u are directly related to the corresponding θ-profiles. The near-singular velocity cusp evident in figure 7(*a*) (i) is characteristic of thermocapillary flows discussed by Zebib, Homsy & Meiburg (1985). Although the velocity cusp resembles a discontinuity in the solution, the velocity does fall to zero as the wall is approached. For most parameter combinations, the velocity cusp is resolved (i.e. at least one grid point lies between the wall and the grid location of the cusp). For some simulations, however, the cusp is at the first grid location inside the domain. Although the cusp may not be fully resolved for these parameter combinations, mesh resolution studies have confirmed the adequacy of the chosen grid and have shown that this cusp has negligible impact on the rest of the flow.

The oscillation described above relies on a tight coupling between sensitivity of the surface to cooling and the influence of the cool finger. One measure for the range of influence of the cool finger is extracted from the profiles of θ_t. Surface profiles of θ_t at instants $\frac{1}{2}\pi$ and $\frac{3}{2}\pi$, figure 7(*b*) iii), show a characteristic intersection near zero. The horizontal location of this point is denoted x_θ and is tabulated in table 3. Consistency in the displacement of x_θ with increasing Ma suggests that this point may be associated with the thermal perturbation caused by the cool finger. The value of x_θ is plotted as a function of the Ma in figure 8 for the aspect ratio 2.6 simulations. A near linear

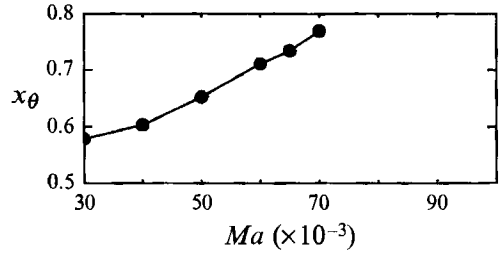

FIGURE 8. Horizontal location, x_1, of the fluctuating temperature, θ_t, cross-over point as a function of the Marangoni number for aspect ratio 2.6.

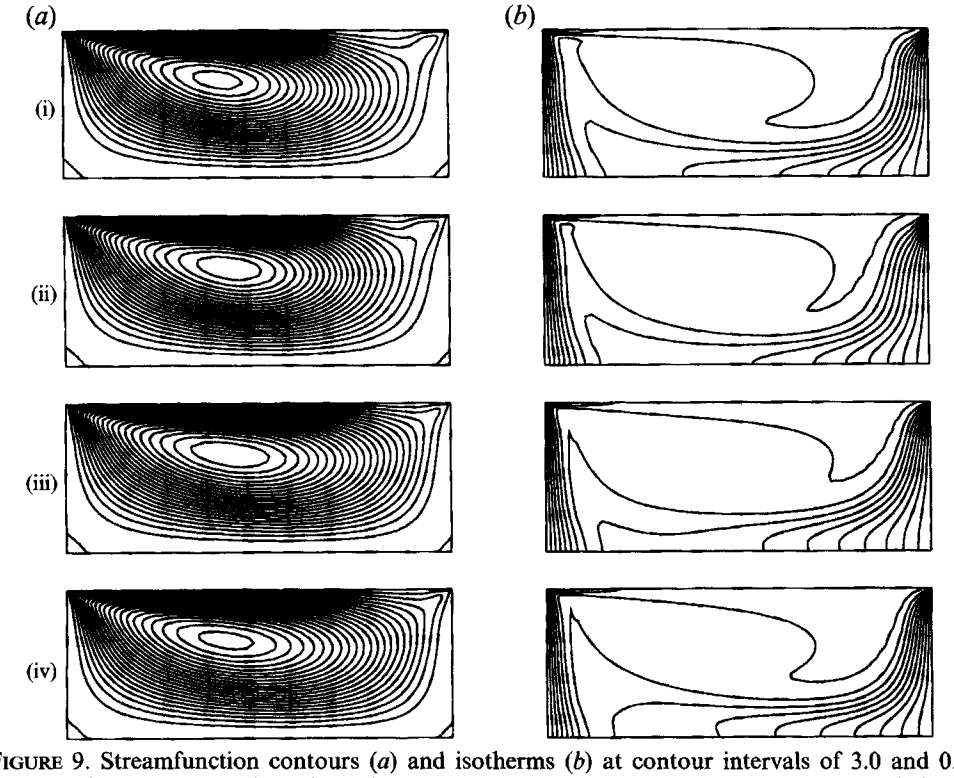

FIGURE 9. Streamfunction contours (*a*) and isotherms (*b*) at contour intervals of 3.0 and 0.0625, respectively, over one period of oscillation for (Ar, Ma) = (2.6, 70000): samples from (i) $\frac{1}{2}\pi$, (ii) π, (iii) $\frac{3}{2}\pi$, and (iv) 2π.

displacement of x_θ along the interface is evident with increasing Ma, figure 8, lending evidence to the idea that increased convection in the primary cell moves the most cooling sensitive region of the interface toward the cold wall and away from the influence of the cold finger.

As convection increases and the influence of the cool finger on the surface is diminished, $\Delta\psi$ decreases and the upper critical branch is approached. Results for the parameter combination (2.6, 70000) near the upper critical curve are presented in figure 9. Although strong secondary and tertiary cells are seen in the (2.6, 50000) simulation, time-dependent parameter combination (2.6, 70000) does not show these structures confirming that the secondary and tertiary cells are an effect of the specific convection field and are not mechanistic features of the oscillation.

Near the upper branch of the stability curve, the nature of the thermocapillary

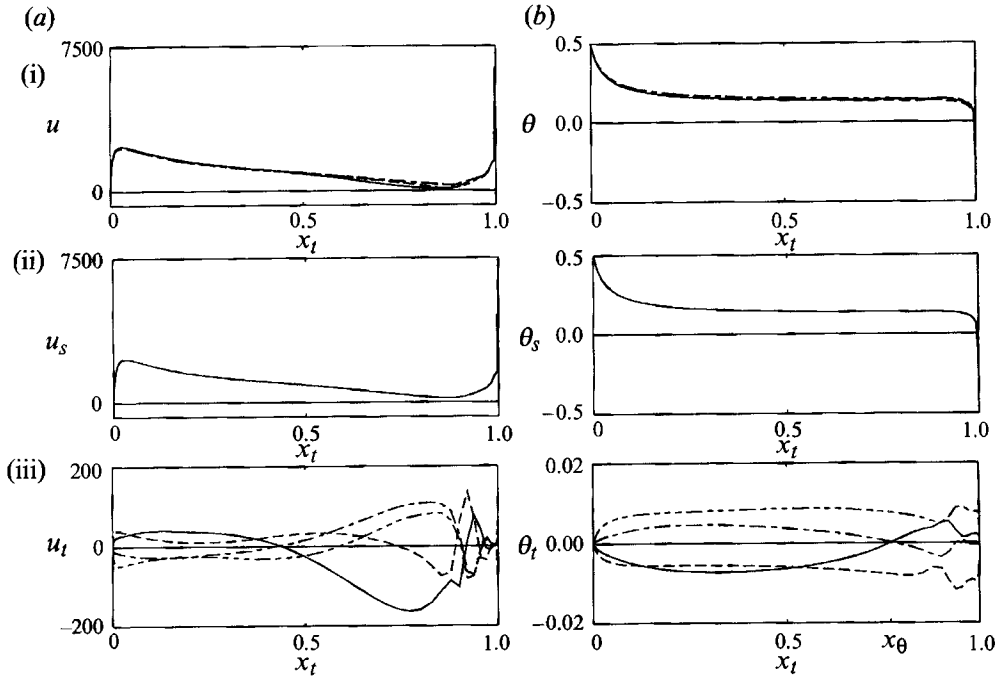

FIGURE 10. Surface profiles of horizontal velocity (*a*) and temperature (*b*) for (*Ar*, *Ma*) = (2.6, 70000) sampled at instants ——, $\frac{1}{2}\pi$, – – –, π, —·—, $\frac{3}{2}\pi$ and —··—, 2π in the oscillation period: (i) total quantity, (ii) average, and (iii) fluctuation from average.

response is dominated by the penetration of the primary convection cell deep into the cavity throughout the oscillation cycle. The time-dependence is characterized by small accelerations and decelerations of the primary convection cell caused by minute deflections of the surface temperature profile, figure 10(*b*) (i). The existence of x_θ is also clearly seen in figure 10(*b*) (iii).

At the upper stabilization near $Ma_c = 80000$, the primary convection cell becomes so strong that the cooling sensitive region of the surface is moved beyond the influence of the cool thermal finger. The streamfunction contours and isotherms for simulations above $Ma = 70000$ differ only marginally from figure 9(ii).

The geometry of the primary convection cell for high *Ar* simulations is bounded by the depth of the cavity; therefore, the ability of the cell to transport x_θ away from the influence of the cool finger is limited. This is clearly seen in the data for the $Ar = 3.8$ simulations presented in table 3. Here, x_θ stabilizes near 0.5 with increasing *Ma* and the upper arm of the stability diagram cannot exist. We project from our data that the critical *Ar* above which the upper arm of the stability diagram will not exist is near 3.

Streamfunction contours and isotherms for the lower critical parameter combination (2.8, 30000) are presented in figure 11. The structural features obtained for oscillatory cases are also present in this figure. The lower branch of the stability curve is reached when the primary convection cell becomes sufficiently strong; for this condition. x_θ is closest to the hot wall (figure 8).

4.3. *Interpretation of the stability results for physical systems*

In this section, we interpret the stability results for layers of water, acetone, and sodium nitrate for the ranges of (*Ar*, *Ma*) represented in figure 3. In particular, we concentrate on the *Ar* range between 2.3 and 3.8 and the *Ma* range between 3×10^4 and 10^5 within

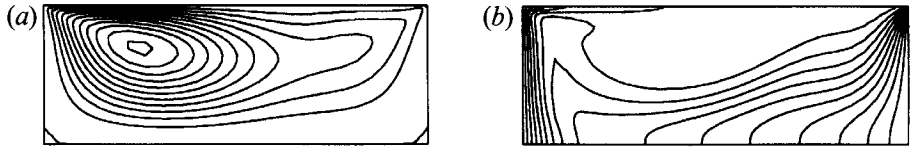

FIGURE 11. Streamfunction contours (*a*) and isotherms (*b*) at contour intervals of 3.0 and 0.0625, respectively, for (*Ar*, *Ma*) = (2.8, 30000).

which the oscillatory regime is found. The stability diagram was constructed for a *Pr* identical to the *Pr* for water, 6.78, however, the values of *Pr* for acetone and sodium nitrate, 3.73 and 8.86, are different. Still we expect that the behaviour of the stability diagram is approximately valid for these fluids.

For a particular fluid, three-environmental variables are incorporated in an (*Ar*, *Ma*) pair. These are L_x, L_y, and ΔT. Therefore, for a particular (*Ar*, *Ma*) combination, there is only one independent variable. Also, the ratio of thermodynamic variables expressed in *Ma* is simply a constant of proportionality relating *Ma* to the environmental variables. For water, acetone, and sodium nitrate, this constant of proportionality is 1.18×10^6, 3.48×10^6, and 1.17×10^5, respectively.

We assume that the Boussinesq equations are valid for $\Delta T \leqslant 4$ °C, thus for a cavity 38 mm long the oscillatory response could be explored experimentally using either water or acetone as the working fluid. For example, a layer of water would experience the evolution from transition to oscillatory convection through restabilization within a range of ΔT between 0.445 °C and 2.22 °C. The same effects for acetone would be found in the smaller range of ΔT between 0.151 °C and 0.753 °C. Since the independent parameter in the non-dimensionalization is the combination $\Delta T L_x$, a ΔT range of larger magnitude could be constructed for acetone by decreasing the length of the cavity. Sodium nitrate, on the other hand, would require a ΔT range between 4.51 °C and 22.5 °C which is beyond the acceptable bounds. If we fix ΔT at 3 °C, however, the transition to oscillatory convection through restabilization could be explored in cavities with lengths between 5.71 cm and 28.5 cm. Using acetone or water, however, cavities with lengths as small as 1.91 mm would be necessary to satisfy this ΔT.

5. Conclusions

The present study is the first to find oscillatory thermocapillary convection using full numerical simulation assuming a flat free surface. These results support the theoretical work by Smith & Davis (1983) considering a thermal–convective mechanism for instability by showing that a sustained oscillation can be elicited in the cavity without surface deformation. We also provide indirect support for the *Pr* dependence of the instability as described by Smith & Davis (1983). We were able to capture the oscillatory instability using a two-dimensional cavity and a moderate *Pr* working fluid. According to Smith & Davis (1983), the instability for a $Pr = 6.78$ fluid should propagate predominantly (nearly 80%) in the plane we consider. The corresponding instability for small *Pr* fluids is predicted to propagate perpendicular to the computational domain and would not be captured by our two-dimensional simulation. Ben Hadid & Roux (1990) sought time-dependence in such a two-dimensional cavity for a low *Pr* fluid and were unable to find oscillatory behaviour in agreement with Smith & Davis (1983).

A stability diagram is developed for a $Pr = 6.78$ fluid demarcating a regime of time-dependent thermocapillary convection in (*Ar*, *Ma*) space. This diagram predicts both

a minimum critical Ar near 2.3 and a minimum Ma_c near 20000 within the parameter ranges spanned by this study. Below either of these values, steady convection will be observed for all parameter combinations. Over a range of parameters, both a lower branch and an upper branch of the stability curve are found. In these ranges, stability with respect to time-dependence is found for both low and high values of the control parameter. A second critical Ar is also suggested near 3.0 above which the upper branch of the stability curve may not exist. This is probably due to the influence of depth on the geometry of the primary convection cell.

The lower branch of the stability curve predicts a range of Ma_c between 20000 and 40000 for Ar values between 2.3 and 3.8. This range of Ma_c agrees well with experimental estimates ranging from 20000 to 30000 (Preisser *et al.* 1983; Kamotani *et al.* 1984). The dependence of Ma_c on Ar has also been experimentally demonstrated (Velten *et al.* 1991).

A complete analogy is found for the evolution of large-scale structures in the flow field with increasing Ma or decreasing Ar. These are related to increases in the strength of the flow with either increasing thermocapillarity or decreasing viscous dissipation.

A description of the oscillatory instability is offered relating the temporal evolution of large-scale structures in the flow and their interaction with the temperature sensitive free surface. This description agrees with Smith (1986), however, here, the origin of the thermal perturbation at the free surface is related to the evolution of a cool finger of fluid from the cold wall convected beneath the large central eddy. For instability, the cooling sensitive region of the surface must lie within the influence of this cool finger, thus the cool finger alone is not sufficient to invoke oscillation. The transition to oscillatory thermocapillary flow occurs when fluid motion becomes sufficiently strong that the cool finger surfacing near the hot wall is able to influence the thermocapillary surface.

Far from near-critical parameter combinations, large-scale structural changes over the oscillation cycle lead to high-amplitude oscillations. For these, the cavity decomposes into thermocapillary and inertially dominated regimes. The flow field is distinguished by primary, secondary and tertiary convection cells.

For large Ar cavities, the dimensions of the primary convection cell are determined by the depth of the fluid layer. It is possible that the primary cell may not be able to transport the temperature sensitive region of the surface beyond the influence of the subsurface cooling. The upper branch of the stability curve would not exist for such a flow. This condition is suggested in the stability diagram by the second critical Ar near 3.0 and is also supported by data for x_θ which probably corresponds to the position of the temperature sensitive region of the interface. For the $Ar = 3.8$ simulations, x_θ stabilizes at a constant value near 0.5 with increasing Ma.

The authors would like to thank Dr J. N. Koster for helpful discussions concerning this work, and M. Farhangnia for appreciated assistance in preparing the manuscript.

This work was conducted while L.J.P. was supported by the NASA Graduate Researchers Program through NASA/Lewis Research Center. Support was also provided by NASA Grant no. NAG3-1094.

A list of material properties used in this study is available from the authors.

REFERENCES

Ben Hadid, H. & Roux, B. 1990 Thermocapillary convection in long horizontal layers of low-Prandtl-number melts subject to a horizontal temperature gradient. *J. Fluid Mech.* **221**, 77–103.

BEN HADID, H. & ROUX, B. 1992 Buoyancy- and thermocapillary-drive flows in differentially heated cavities for low-Prandtl-number fluids. *J. Fluid Mech.* **235**, 1–36.

BIRINGEN, S. & DANABASOGLU, G. 1989 Oscillatory flow with heat transfer in a square cavity. *Phys. Fluids* A **1** (11), 1796–1812.

CARPENTER, B. M. & HOMSY, G. M. 1990 High Marangoni number convection in a square cavity: Part II. *Phys. Fluids* A **2** (2), 137–149.

CHUN, CH.-H. 1980 Experiments on steady and oscillatory temperature distribution in a floating zone due to the Marangoni convection. *Acta Astronautica*, **7**, 479–488.

GHIA, U., GHIA, K. N. & SHIN, C. T. 1982 High-*Re* solutions for incompressible flow using the Navier–Stokes equations and a multigrid method. *J. Comput. Phys.* **48**, 387–411.

HUSER, A. & BIRINGEN, S. 1992 Calculation of two-dimensional shear-driven cavity flows at high Reynolds numbers. *Int. J. Numer. Meth. Fluids* **14**, 1087–1109.

JURISCH, M. 1990 Surface temperature oscillations of a floating zone resulting from oscillatory thermocapillary convection. *J. Cryst. Growth* **102**, 223–232.

KAMOTANI, Y., OSTRACH, S. & VARGAS, M. 1984 Oscillatory thermocapillary convection in a simulated floating-zone configuration. *J. Cryst. Growth* **66**, 83–90.

KIM, J. & MOIN, P. 1985 Application of a fractional-step method to incompressible Navier–Stokes equations. *J. Comput. Phys.* **59**, 308–323.

LE, H. & MOIN, P. 1991 An improvement of fractional step methods for the incompressible Navier–Stokes equations. *J. Comput. Phys.* **92**, 369–379.

SHEN, Y., NEITZEL, G. P., JANKOWSKI, D. F. & MITTELMANN, H. D. 1990 Energy stability of thermocapillary convection in a model of the float-zone crystal-growth process. *J. Fluid Mech.* **217**, 639–660.

PELTIER, L. J. 1992 Numerical simulation of time-dependent thermocapillary convection in layered fluid systems. Ph.D thesis, University of Colorado.

PELTIER, L. J., BIRINGEN, S. & CHAIT, A. 1990 Application of implicit numerical techniques to the solution of the three-dimensional diffusion equation. *Numer. Heat Transfer, Part B*, **18**, 205–219.

PELTIER, L. J. & BIRINGEN, S. 1992 Time-dependent thermocapillary convection in a Cartesian cavity: numerical simulation of encapsulated fluid systems. To be submitted.

PREISSER, F., SCHWABE, D. & SCHARMANN, A. 1983 Steady and oscillatory thermocapillary convection in liquid columns with free cylindrical surface. *J. Fluid Mech.* **126**, 545–567.

PULICANI, J. P., CRESPO DEL ARCO, E. & PEYRET, R. 1990 Spectral simulations of oscillatory convection at low Prandtl number. *Intl J. Numer. Meth. Fluids* **10**, 481–517.

SEN, A. K. & DAVIS, A. H. 1982 Steady thermocapillary flows in two-dimensional slots. *J. Fluid Mech.* **121**, 163–186.

SHEN, Y., NEITZEL, G. P., JANKOWSKI, D. E. & MITTELMAN, H. D. 1990 Energy stability of thermocapillary convection in a model of the float zone crystal-growth process. *J. Fluid Mech.* **218**, 639–660.

SMITH, M. K. 1986 Instability mechanisms in dynamic thermocapillary liquid layers. *Phys. Fluids* **29** (10), 3182–3186.

SMITH, M. K. 1988 The nonlinear stability of dynamic thermocapillary liquid layers. *J. Fluid Mech.* **194**, 391–415.

SMITH, M. K. & DAVIS, S. H. 1983 Instabilities of dynamic thermocapillary liquid layers. Part 1. Convective instabilities. *J. Fluid Mech.* **132**, 119–144.

DE VAHL DAVIS, G. 1983 Natural convection in a square cavity: a bench mark numerical solution. *Intl J. Numer. Meth. Fluids* **3**, 249–264.

VELTEN, R., SCHWABE, D. & SCHARMANN, A. 1991 The periodic instability of thermocapillary convection in cylindrical liquid bridges. *Phys. Fluids* A **3** (2), 267–279.

VILLERS, D. & PLATTEN, J. K. 1992 Coupled buoyancy and Marangoni convection in acetone: experiments and comparisons with numerical simulations. *J. Fluid Mech.* **234**, 487–510.

XU, J.-J. & DAVIS, S. H. 1984 Convective thermocapillary instabilities in liquid bridges. *Phys. Fluids* **27** (5), 1102–1107.

ZEBIB, A., HOMSY, G. M. & MEIBURG, E. 1985 High Marangoni number convection in a square cavity. *Phys. Fluids* **28** (12), 3467–3476.